Available online at www.sciencedirect.com
SCIENCE DIRECT®
Journal of Solid State Chemistry 178 (2005) 715–728
JOURNAL OF SOLID STATE CHEMISTRY
www.elsevier.com/locate/jssc

Ba_6Ge_{25}: low-temperature Ge–Ge bond breaking during temperature-induced structure transformation

Wilder Carrillo-Cabrera*, Horst Borrmann, Silke Paschen, Michael Baenitz, Frank Steglich, Yuri Grin

Max-Planck-Institut für Chemische Physik fester Stoffe, Nöthnitzer Str. 40, D-01187 Dresden, Germany

Received 10 September 2004; received in revised form 10 November 2004; accepted 11 November 2004

Abstract

In order to find the optimal conditions for sample preparation of the binary germanide Ba_6Ge_{25}, the germanium-rich part of the Ba–Ge phase diagram was redetermined by means of metallography, X-ray powder diffraction and differential thermal analysis. The temperature behavior of cubic Ba_6Ge_{25} was investigated both on polycrystalline samples and single crystals. The temperature dependence of the lattice parameter exhibits two anomalies at about 180 and 230 K, respectively, which are caused by a structure transformation in two steps with hysteresis. Powder ($T = 10$–295 K) and single-crystal ($T = 95$–295 K) X-ray diffraction studies confirm that the symmetry of Ba_6Ge_{25} (space group $P4_132$) remains unchanged within the entire temperature range. A reconstructive behavior of the structural transformation is observed, involving Ge–Ge bond breaking and barium cation displacements. Some Ge4 type atoms (~28%) are so significantly displaced during cooling that Ge4–Ge6 bonds break and new three-bonded (3b)Ge^- species (electron acceptors) are formed. Consequently, the number of charge carriers is reduced, affecting the physical properties. The reversible bond breaking involved in this process is a typical characteristic of a solid-state chemical reaction.

Keywords: Ba_6Ge_{25}; Phase transition; Reconstructive transformation; Split sites; Ge–Ge bond breaking; Lone-pairs; Dangling bonds; Binary Ba–Ge system

1. Introduction

Ba_6Ge_{25} belongs to the structure family of chiral clathrates with Pearson symbol *cP*124 (space group $P4_132$) [1–3], being a binary prototype of the $Ba_6In_4Ge_{21}$ structure type [4,5]. Ba_6Ge_{25} exhibits a lattice parameter of $a = 14.5564(2)$ Å at ambient temperature [1] and each unit cell contains four formula units. The crystal structure is characterized by a three-dimensional (3D) arrangement of condensed Ge_{20} pentagonal dodecahedra. The arrangement is not space-filling, showing a zeolite-like 3D channel system (Fig. 1a). Part of the 3D germanium framework are helices of face-sharing pentagonal dodecahedra (*pdo*) along {100} directions. At ambient temperature, the average Ge–Ge distance is 2.53(4) Å, which is larger than the corresponding one in the diamond-type structure of germanium (2.44 Å). There are three non-equivalent crystallographic positions for the barium atoms, which are labelled as Ba1 (8*c* site; two atoms per formula unit Ba_6Ge_{25}), Ba2 (12*d*; three per formula unit) and Ba3 (4*a*; one per formula unit). The germanium atoms occupy six crystallographically non-equivalent positions, i.e. Ge1 (24*e* site), Ge2 (8*c*), Ge3 (8*c*), Ge4 (12*d*), Ge5 (24*e*) and Ge6 (24*e*) [1].

The Ba3 site is the most peculiar barium position as it has only 11 germanium nearest neighbors in contrast to Ba1 and Ba2, both having 20 germanium neighbors. As illustrated in detail in Fig. 1b, the germanium environment around Ba1 is a Ge_{20} pentagonal dodecahedron (Ba1 *pdo*). In the zeolite-like labyrinth, Ba2 occupies a

*Corresponding author. Fax: +49 351 4646 3002.
E-mail address: carrillo@cpfs.mpg.de (W. Carrillo-Cabrera).

0022-4596/$ - see front matter © 2004 Elsevier Inc. All rights reserved.
doi:10.1016/j.jssc.2004.11.011

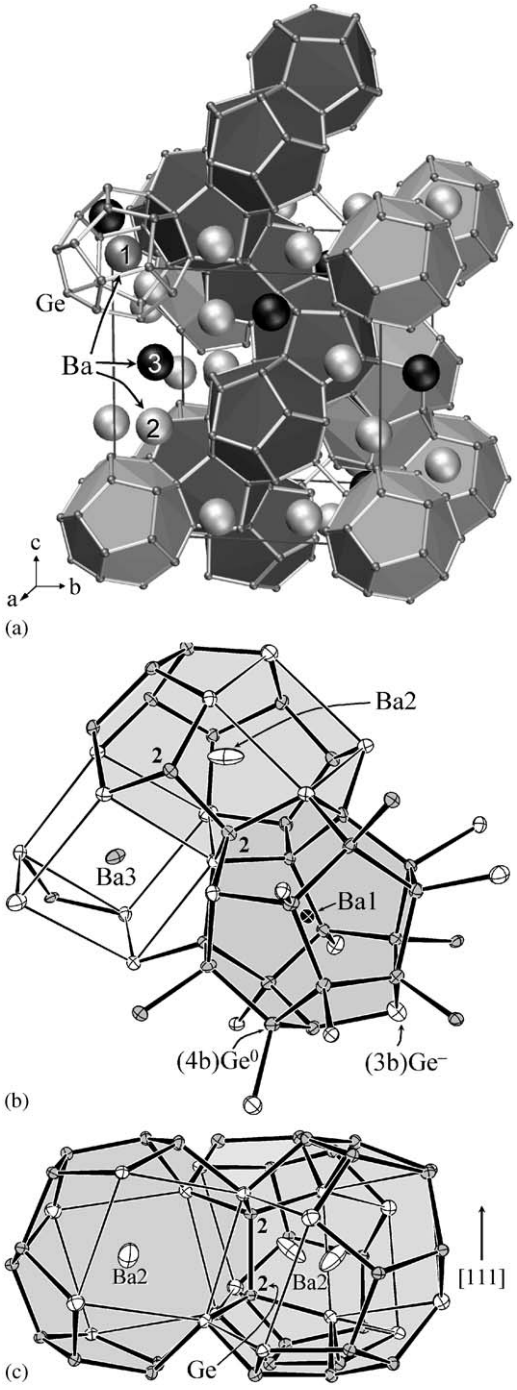

Fig. 1. Crystal structure of Ba_6Ge_{25}. (a) Framework of condensed Ge_{20} pentagonal dodecahedra (*pdos*). A helical fragment of face-sharing *pdos* along [001] is emphasized in dark. (b) Germanium environments around Ba1 (Ba1 *pdo*), Ba2 (Ba2 *polyh*) and Ba3 (Ba3 *cube*). (c) Three condensed Ba2-*polyh*s sharing a common Ge2–Ge2 edge parallel to [111]. In (b) and (c) ellipsoids are drawn at 60% probability level. Thick sticks represent Ge–Ge bonds. Thin lines are added for clarity only.

distorted Ge_{20} polyhedron (Ba2 *polyh*) composed of six pentagonal faces and two large square faces (windows). Ba3 is located in a *cube*-like Ge_8 cavity (Ba3 *cube*) composed of six large windows with three more distant Ge atoms (Ge4) bridging three edges of the *cube* (angles of the distorted *cube* are in the range 82–97°). Three condensed Ba2 *polyhs* share a common Ge2–Ge2 edge oriented along [111] (Fig. 1c).

The most peculiar structural characteristic of Ba_6Ge_{25} is that 32 (8 per formula unit) out of 100 Ge atoms in the unit cell are three-bonded (3b), each accommodating a lone-pair and acting as charge-acceptor. According to the Zintl-Klemm concept [6,7], these are formally considered as $(3b)Ge^-$ ions (located at the Ge3 and Ge5 sites). The remaining 68 Ge atoms (17 per formula unit) are four-bonded (4b) neutral species (labelled as $(4b)Ge^0$ in Fig. 1b). Assuming two-centre two-electron Ge–Ge bonds, the formal charge balance in Ba_6Ge_{25} can be written as $[Ba^{2+}]_6[(3b)Ge^-]_8[(4b)Ge^0]_{17}[4e^-]$ [1]. Thus, four excess electrons per formula unit are expected, suggesting n-type conductivity with a nominal charge-carrier concentration of about $5.2\times10^{21}\,cm^{-3}$.

In recent years the Ba_6Ge_{25} clathrate has attracted considerable scientific interest because of its unusual physical properties. Based on the measurement of transport properties [8] and the structural findings in a preliminary low-temperature X-ray powder investigation [9] it was concluded that Ba_6Ge_{25} undergoes a two-step structural phase transition at about 230 and 180 K upon cooling, accompanied by a pronounced thermal hysteresis and inducing dramatic changes in the transport properties. Above the transition temperature the electrical conductivity is metal-like. At 230 K the electrical resistivity starts to increase with decreasing temperature and at 180 K it increases abruptly. By decreasing the temperature further, the electrical resistivity continues to increase gradually and finally saturates at very low temperatures.

The n-type conductivity was confirmed by Hall effect measurements [8] which (within a one-band model approximation) indicated that the amount of electron-like carriers increases from $8\times10^{21}\,cm^{-3}$ at 2 K to $1.7\times10^{22}\,cm^{-3}$ at 400 K (about 6–13 electrons per Ba_6Ge_{25} formula unit). Apart from the generally strong temperature dependence of the carrier concentration, a distinct increase of about 1.5 electrons per formula unit was observed across the phase transformation (180–240 K) in the warm-up cycle.

Another unusual effect of the phase transformation was the drop of magnetic susceptibility $\chi(T)$ in the range 180–240 K [8]. The drop occurs in two steps and from comparison of cooling and warm-up sweeps again a thermal hysteresis effect was observed. Based on chemical bonding models, the compound was expected to be a Pauli paramagnet, however, the magnetic susceptibility $\chi(T)$ was found to be negative through the entire temperature range (2–400 K). A possible reason for the negative $\chi(T)$ may be an additional diamagnetic contribution, which accounts for the

molecular ring current induced in the germanium framework by the Lorentz force within a magnetic field [8].

Specific heat $c_p(T)$ measurements showed a symmetrical anomaly between 190 and 260 K with a maximum at 223 K, a rather wide peak. It was also deduced that the transformation has an unusually large entropy contribution ($1.47R$ per mol Ba_6Ge_{25}, where R is the universal gas constant) [8].

In consecutive studies [10–12] it was shown that Ba_6Ge_{25} is a superconductor. Hydrostatic pressure suppresses the structural phase transition. At 2.8 GPa the electrical resistivity shows a metal-like behavior within the entire temperature range. More interestingly, the superconducting transition temperature (T_c) increases with increasing pressure from $T_c = 0.24$ K at ambient pressure to $T_c = 3.85$ K at $p = 2.8$ GPa. The maximum of this remarkable enhancement ($\sim 16\times$) is associated with the complete suppression of the structural phase transition at 2.8 GPa.

Analysis of our preceding low-temperature X-ray powder diffraction data on Ba_6Ge_{25} [9] indicated that the cubic symmetry of Ba_6Ge_{25} is maintained in the whole temperature range (10–295 K), and that the Ba2 and Ba3 positions displayed pronounced atomic displacements during the transition (this was confirmed by independent investigations on powder samples [13]). However, variation in the germanium framework is difficult to be recognized from powder data. We therefore decided to carry out X-ray diffraction experiments at low temperatures on single crystals.

The temperature dependence of the lattice parameter as derived from a powder sample, the results of the single-crystal diffraction experiments, interpretation and relationship between structural and physical property anomalies of Ba_6Ge_{25} are presented here. The phase relationship in the Ge-rich region of the Ba–Ge phase diagram (region of existence for Ba_6Ge_{25} and Ba_8Ge_{43} [14,15]) are also described in detail in order to establish the stability range and composition of Ba_6Ge_{25}. These new experiments show that the germanium substructure plays a very important role in the phase transition, and a new view of this complex process is established.

2. Experimental

2.1. Preparation and thermal analyses

To determine the Ba–Ge phase diagram, samples (2–3 g) with nominal compositions in the range $Ba_{0.33}Ge_{0.67}$ to $Ba_{0.10}Ge_{0.90}$ were prepared from the elements in open glassy carbon crucibles (high-frequency induction furnace) in an argon-filled glove box ($O_2 < 1$ ppm, $H_2O < 1$ ppm). Annealing to achieve sample homogenization was performed in evacuated quartz glass ampoules followed by quenching in water. To avoid reaction with the quartz glass ampoule, each sample was wrapped in molybdenum foil (for heat treatments at temperatures below 660 °C) or inserted in a glassy carbon crucible (for temperatures above 660 °C). Samples were annealed at 650 and 795 °C for several days (7–30 days). The final heat treatment of the Ba_6Ge_{25} sample used in all experiments (physical properties, powder and single-crystal X-ray diffraction) was annealed at 650 °C for 12 days. Differential thermal analysis (DTA) was done on bulk samples (60–120 mg) in a protective argon atmosphere with a heating rate of 2 °C/min (Netzsch STA 409 EP). DTA experiments were performed on a series of Ba_xGe_{1-x} alloys ($x = 0.10$–0.33) after annealing at 650 °C. Differential scanning calorimetry (DSC; Netzsch STA 409C/CD; ~60 mg; argon atmosphere, heating rate 5 °C/min) was carried out only on Ba_6Ge_{25} in order to determine the transition temperatures.

2.2. Metallographical and chemical analyses

Specimens for metallographic (conventional optical microscope) and SEM (Philips XL30 SEM) investigations were polished using standard methods without final etching (samples were sufficiently stable in air or moisture). The optical micrographs were obtained using differential interference contrast and partially polarized light.

Chemical analyses were performed by EDXS (Philips XL30 SEM) or ICP-AES (Varian Vista RL) methods.

2.3. X-ray diffractometry

The X-ray powder diffraction intensities were collected on a Huber image plate Guinier camera G670 ($CuK\alpha_1$ radiation, $\lambda = 1.540562$ Å) at ambient temperature for all samples used in the phase diagram redetermination, but also in the temperature range 10–295 K for Ba_6Ge_{25}. In ambient temperature measurements, LaB_6 was used as internal standard ($a = 4.15695(6)$ Å). The cooling and heating rates during the temperature dependent experiments were 5 K/h, but before the start of the measurement at a given temperature, the sample was left at this temperature for at least 30 min. Special care was taken in the respective temperature range to account for the hysteresis effects. The lattice parameters were calculated from powder data using the program package WinCSD [16].

Several single crystals (extracted mechanically from the same Ba_6Ge_{25} batch used for the physical measurements) were tested and the one considered best was chosen for single-crystal X-ray diffraction experiments carried out on a Stoe IPDS equipment (AgK_α radiation, $\lambda = 0.56087$ Å) at temperatures in the range 95 to 295 K. Cooling and heating rates were again 5 K/h, but to

assure equilibrium the sample was kept at a given temperature for about 3 h before data collection. A total of 26 data sets was collected and analysed. The lattice parameters determined by X-ray powder diffraction methods were used within the respective crystal structure refinement. However, because of a systematic shift in the powder data observed in the warm-up sweep from 225 to 295 K, the lattice parameter values refined in this range from the initial cool-down cycle were used instead (see Results and Discussion).

Absorption effects were corrected numerically using the program X-RED [17]. Structure refinement was performed using the full-matrix least-squares program SHELXL-97 [18]. Extinction effects were hardly discernible and therefore no correction was applied. For each data set, all reflections measured within $2\theta \leqslant 54^\circ$ ($-23 \leqslant h, k, l \leqslant 23$) were used in the structure refinement. Difference electron density maps (using experimental data) were calculated with the Fourier calculation program FOURIER_MAP of the WinGX package [19], and corresponding 3D isosurfaces were smoothed and visualized with the program MAPVIEW of the same package.

3. Results and discussion

The main emphasis of this work is on the structural phase transformation of Ba_6Ge_{25} at low temperatures to better understand its unusual physical properties. However, at the beginning of this study, the exact composition of the compound was still an open question. This fact became even more important to us when a composition $Ba_6Ge_{24}\square_1$ (one germanium vacancy per formula unit) was proposed in a recent article [3].

3.1. Phase relationships

The existence of a phase with composition "$BaGe_4$" had already been known since 1970 [20] and had also been reported in ternary phase diagrams, e.g. in the Al–Ba–Ge system [21]. In order to prove that "$BaGe_4$" actually is Ba_6Ge_{25}, to determine its stability range and to optimize its preparation conditions, the Ge-rich region of the Ba–Ge phase diagram [20] was re-investigated.

The reconstructed phase diagram is shown in Fig. 2. Ba_6Ge_{25} forms peritectically at 815 °C from $BaGe_2$ and liquid phase. Micrographs of samples with starting compositions Ba_6Ge_{24}, Ba_6Ge_{25} and $Ba_6Ge_{25.7}$ (Fig. 3) reveal that the composition of the phase previously denoted "$BaGe_4$" is indeed Ba_6Ge_{25}, as only this specimen proved to be single-phase. The other two samples (Ba_6Ge_{24} and $Ba_6Ge_{25.7}$) disclosed one additional phase ($BaGe_2$ and Ge in Ba_6Ge_{24} and $Ba_6Ge_{25.7}$ samples, respectively). $BaGe_2$ decomposes in air to form an amorphous red material of larger volume (labeled as "$BaGe_2$" in Fig. 3).

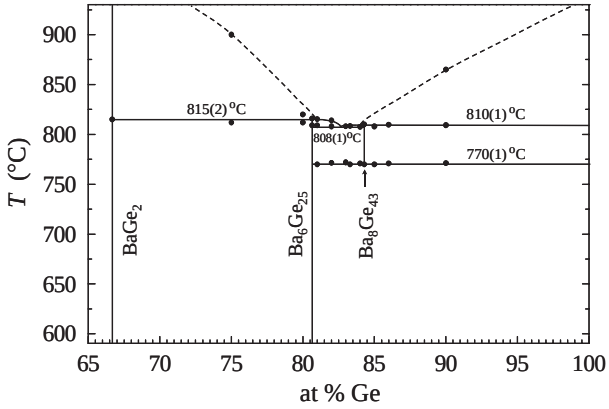

Fig. 2. Revised phase diagram of the Ba–Ge binary system in the germanium-rich region. (In phase diagrams temperatures are commonly given in °C.)

The ICP-AES analyses of the single-phase sample Ba_6Ge_{25} revealed a composition $Ba_{5.98(6)}Ge_{25.02(9)}$. The Ba_6Ge_{25} lattice parameters for this sample (14.5564(2) Å) as well as for two-phase samples at either side of Ba_6Ge_{25} are equal within standard deviations (14.5562(2) Å and 14.5561(2) Å for $Ba_6Ge_{25.7}$ and Ba_6Ge_{24}, respectively). This confirms that Ba_6Ge_{25} exhibits no significant homogeneity range.

In the temperature range 770–810 °C, Ba_6Ge_{25} is in equilibrium with the high-temperature phase Ba_8Ge_{43}. EDX analysis (composition $Ba_{8.0(1)}Ge_{42.9(1)}$), X-ray powder diffraction study as well as the X-ray single-crystal structure determination revealed that this clathrate-I type phase has only three vacancy sites per formula unit: $Ba_8Ge_{43}\square_3$ [22].

3.2. Crystal structure

The temperature dependence of the lattice parameter $a(T)$ of Ba_6Ge_{25} is shown in Fig. 4a. Upon cooling from room temperature, $a(T)$ first decreases until about 230 K ($\Delta a = -0.0151$ Å), but shows an anomalous two-step increase between 225 and 175 K, raising first by $\Delta a = +0.0024$ Å from 230 to 210 K, and after being almost constant between 210 and 185 K it increases rapidly between 185 and 175 K by $\Delta a = +0.0056$ Å. Derived transition temperatures are T_{S1}, T_{S2}(down) $\approx$230, 180 K. Below 175 K ($a = 14.5502(2)$ Å) the lattice parameter decreases with temperature down to $a = 14.5338(2)$ Å at 10 K ($\Delta a = -0.0164$ Å). The variation of the lattice parameter as function of temperature is reversible, but hysteresis is observed between 180 and 230 K. The overall lattice expansion between 10 and 295 K is only 0.16% (0.0226 Å). During warm-up, the

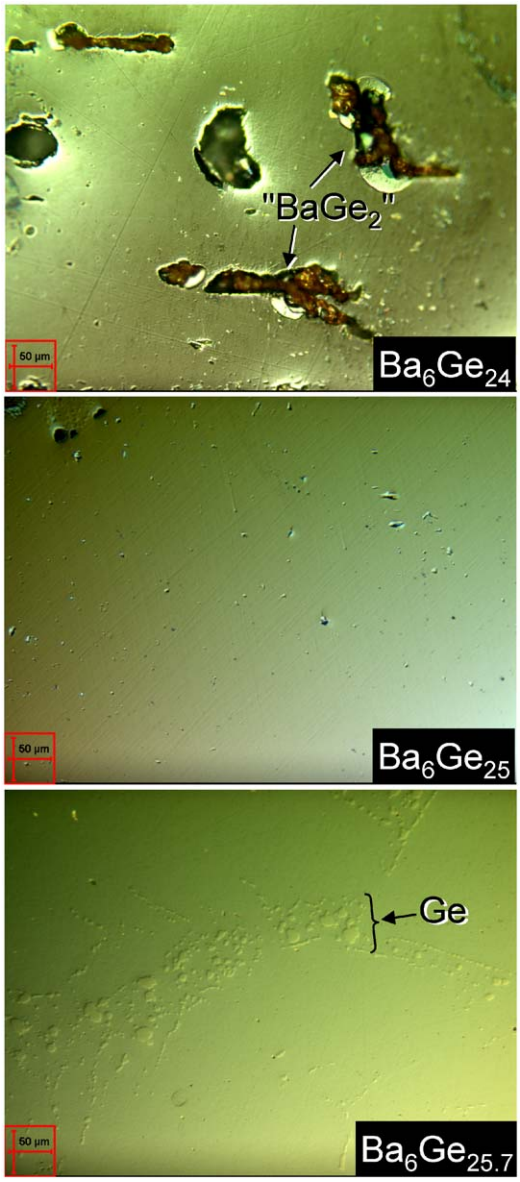

Fig. 3. Microstructure of samples Ba_6Ge_{24} (*top*), Ba_6Ge_{25} (*middle*) and $Ba_6Ge_{25.7}$ (*bottom*); bright-field images using differential interference contrast and partially polarized light.

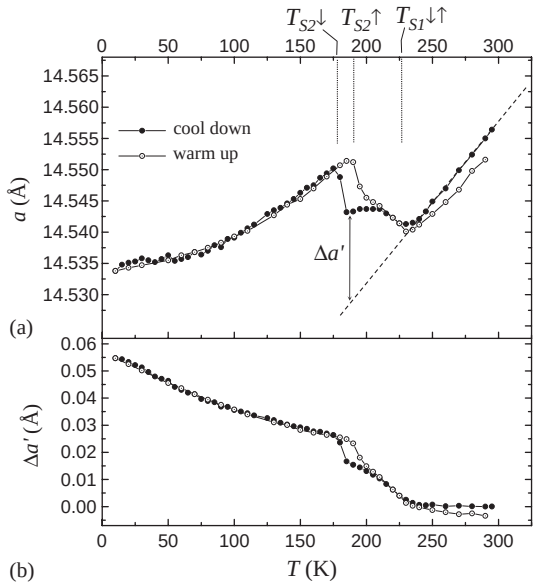

Fig. 4. (a) Lattice parameter a of Ba_6Ge_{25} as a function of temperature, and (b) $\Delta a'$ versus T.

total expansion between 185 and 230 K is already 0.0113 Å (~0.08%), accounting for 50% of the total expansion between 10 and 295 K, a small but remarkable anomaly. In the warm-up sweep the transition temperatures $T_{S1,S2}$(up) are approximately 230 and 190 K, respectively. The disagreement between the $a(T)$ values for heating and cooling cycles in the range 230–295 K is probably due to a slight sample shift during the warm-up sweep, which could not be sufficiently corrected during refinement of the lattice parameter.

In the hypothetical case that no phase transformation occurs, the temperature dependence of $a(T)$ for $T > 20$ K may be approximated as linear (dashed line in Fig. 4a) according to $a' = a_o + \gamma T$, where $a_o = 14.4764$ Å and $\gamma = 2.711 \times 10^{-4}$ Å K^{-1}. The relative deviation ($\Delta a' = a(T)$–$a'(T)$) from this line reveals more pronounced variations (Fig. 4b) and can be directly compared with relative changes of physical properties.

The residual for symmetry equivalent reflections (R_{int}) at room temperature (49124 reflections) is 0.088 (2275 unique reflections). Respective values obtained from low-temperature data are very similar (see Table 1), indicating that the Laue symmetry is maintained through the phase transformation. However, at temperatures below 225 K, the diffraction patterns showed wider reflections, and very weak diffuse scattering was also observed (this is also characteristic in a pre-martensitic state [23]). These features may be caused by internal stress originating from a slight mismatch between transformed and non-transformed domains. As given in Table 1, the values of $R_{gt}(F)$ and $wR_{all}(F^2)$ increase for temperatures below 225 K. Most likely, our structure model for $T < 225$ K is less accurate, but also the quality of the crystal is obviously reduced below the transition temperature. On heating, the good quality of the crystal was recovered, as indicated by the small values obtained for $R_{gt}(F)$ and $wR_{all}(F^2)$. Crystal quality recovery is not usual for first-order phase transitions, but in the current transition only part of the structure is affected (see below).

The atomic coordinates of the room temperature structure for the cubic Ba_6Ge_{25} phase [1] were used as starting values for structure refinement. As found before [1–3], at room temperature the displacement parameters for Ba2 and Ba3 atoms are relatively large, indicating a

Table 1
Brief crystallographic data and atomic positions for Ba_6Ge_{25} at selected temperatures: ↓ = cooling down; ↑ = warming up[a]

Temperature (K)	258↓	225↓	195↓	165↓	95	145↑	190↑	233↑	257↑	295
Unit cell parameter a (Å)	14.5465(2)	14.5415(2)	14.5437(2)	14.5487(2)	14.5389(2)	14.5448(2)	14.5512(2)	14.5414(2)	14.5463(2)	14.5564(2)
Measured reflections	48899	48677	48732	48850	48912	48986	48931	48866	48944	49023
Independent reflections	2275	2262	2263	2269	2272	2274	2272	2271	2272	2275
Reflections with $I>2\sigma(I)$	2044	2032	2124	2077	2131	2095	2088	2034	2036	2016
R(int)	0.077	0.073	0.081	0.088	0.088	0.089	0.092	0.082	0.083	0.088
Refined parameters	51	55	59	59	59	59	59	55	51	51
$R_{gt}(F)$	0.037	0.040	0.057	0.080	0.085	0.083	0.078	0.040	0.040	0.040
$wR_{all}(F^2)$	0.069	0.074	0.104	0.158	0.171	0.164	0.149	0.074	0.072	0.073
x(Ba1/Ba1′)	0.05996(3)	0.05993(3)	0.0628(6)	0.0642(4)	0.0640(4)	0.0643(4)	0.0643(4)	0.05994(3)	0.05994(3)	0.06000(3)
y(Ba1/Ba1′)	x	x	0.0523(2)	0.0483(2)	0.0479(2)	0.0482(2)	0.0487(2)	x	x	x
z(Ba1/Ba1′)	x	x	0.0642(5)	0.0680(4)	0.0683(3)	0.0680(4)	0.0673(4)	x	x	x
U_{eq}(Ba1) or U_{iso}(Ba1′)	0.0146(1)	0.0141(1)	0.0110(4)	0.0147(6)	0.0116(6)	0.0137(6)	0.0148(6)	0.0142(1)	0.0147(1)	0.0158(1)
Occ(Ba2′)	0.532(3)	0.537(3)	0.425(4)	0.249(4)	0.245(4)	0.250(4)	0.271(4)	0.540(3)	0.537(3)	0.530(3)
y(Ba2′)	0.18910(9)	0.1888(1)	0.1878(2)	0.1808(4)	0.1803(4)	0.1806(4)	0.1821(3)	0.1889(1)	0.1890(1)	0.1892(1)
U_{iso}(Ba2′)	0.0241(2)	0.0233(3)	0.0225(4)	0.0274(7)	0.0237(7)	0.0262(8)	0.0280(7)	0.0235(3)	0.0242(2)	0.0259(3)
Occ(Ba2″)	0.234(2)	0.231(2)	0.220(2)	0.249(3)	0.245(3)	0.246(3)	0.245(3)	0.230(2)	0.231(2)	0.235(3)
x(Ba2″)	0.1515(2)	0.1526(2)	0.1520(3)	0.1572(4)	0.1579(4)	0.1575(4)	0.1564(4)	0.1523(2)	0.1520(2)	0.1520(2)
y(Ba2″)	0.1909(2)	0.1907(2)	0.1892(3)	0.1860(4)	0.1853(4)	0.1859(4)	0.1865(4)	0.1907(2)	0.1908(2)	0.1908(2)
z(Ba2″)	0.4421(2)	0.4425(2)	0.4421(3)	0.4420(4)	0.4420(4)	0.4421(4)	0.4420(4)	0.4424(2)	0.4422(2)	0.4422(2)
Occ(Ba2‴)	—	—	0.068(2)	0.127(3)	0.133(3)	0.129(3)	0.120(3)	—	—	—
x(Ba2‴)	—	—	0.1890(9)	0.1920(8)	0.1921(7)	0.1918(8)	0.1911(8)	—	—	—
y(Ba2‴)	—	—	0.1996(8)	0.1994(7)	0.1996(7)	0.1994(7)	0.1995(7)	—	—	—
z(Ba2‴)	—	—	0.4611(8)	0.4627(7)	0.4625(7)	0.4629(7)	0.4627(7)	—	—	—
x(Ba3′)	0.36991(8)	0.36959(9)	0.36750(9)	0.3620(1)	0.3615(1)	0.3618(1)	0.3628(1)	0.36978(9)	0.36995(9)	0.3700(1)
U_{iso}(Ba3′)	0.0141(2)	0.0132(3)	0.0148(4)	0.0193(6)	0.0162(6)	0.0185(6)	0.0195(6)	0.0133(3)	0.0144(3)	0.0159(3)
x(Ge1)	0.29255(5)	0.29260(5)	0.29282(7)	0.2933(1)	0.2934(1)	0.2934(1)	0.2933(1)	0.29260(5)	0.29260(5)	0.29257(5)
y(Ge1)	0.95308(5)	0.95310(5)	0.95301(7)	0.9529(1)	0.9529(1)	0.9529(1)	0.9528(1)	0.95313(5)	0.95309(5)	0.95304(5)
z(Ge1)	0.75006(5)	0.75006(5)	0.75038(7)	0.7512(1)	0.7512(1)	0.7512(1)	0.7511(1)	0.75008(5)	0.75002(5)	0.75010(5)
U_{eq}(Ge1)	0.0123(1)	0.0112(1)	0.0109(2)	0.0149(3)	0.0123(3)	0.0141(3)	0.0148(3)	0.0116(1)	0.0123(1)	0.0135(1)
x(Ge2)	0.92457(5)	0.92458(5)	0.92475(7)	0.9251(1)	0.9251(1)	0.9251(1)	0.9250(1)	0.92456(5)	0.92456(5)	0.92458(5)
U_{eq}(Ge2)	0.0118(2)	0.0107(2)	0.0106(3)	0.0132(5)	0.0110(5)	0.0127(5)	0.0135(4)	0.0111(2)	0.0117(2)	0.0131(2)
x(Ge3)	0.21893(6)	0.21880(7)	0.21837(9)	0.2173(1)	0.2172(1)	0.2172(1)	0.2175(1)	0.21891(7)	0.21893(7)	0.21906(7)
U_{eq}(Ge3)	0.0203(3)	0.0194(3)	0.0183(4)	0.0223(6)	0.0190(6)	0.0213(6)	0.0223(6)	0.0195(3)	0.0204(3)	0.0223(3)
Occ(Ge4/Ge4′)	1	0.967(4)	0.877(7)	0.72(1)	0.71(1)	0.71(1)	0.740(9)	0.973(4)	1	1
y(Ge4/Ge4′)	0.83111(5)	0.83127(6)	0.83204(8)	0.8334(2)	0.8335(2)	0.8335(2)	0.8331(1)	0.83122(6)	0.83114(5)	0.83116(5)
U_{eq}(Ge4/Ge4′)	0.0132(2)	0.0110(2)	0.0094(4)	0.0110(7)	0.0089(8)	0.0104(7)	0.0114(7)	0.0113(2)	0.0130(2)	0.0142(2)
Occ(Ge4″)	—	0.0165	0.0615	0.140	0.145	0.145	0.130	0.0135	—	—
x(Ge4″)	—	0.186(4)	0.188(2)	0.194(1)	0.194(1)	0.194(1)	0.193(1)	0.185(5)	—	—
y(Ge4″)	—	0.808(4)	0.808(2)	0.807(1)	0.807(1)	0.808(1)	0.808(1)	0.807(5)	—	—
z(Ge4″)	—	0.028(4)	0.027(2)	0.0236(9)	0.0229(9)	0.024(1)	0.024(1)	0.030(5)	—	—
U_{iso}(Ge4″)	—	0.020	0.026(5)	0.026(3)	0.022(3)	0.025(3)	0.026(3)	0.020	—	—
Occ(Ge5/Ge5′)	1	1	0.877	0.72	0.71	0.71	0.740	1	1	1
x(Ge5/Ge5′)	0.91647(5)	0.91642(6)	0.9168(2)	0.9176(3)	0.9176(3)	0.9176(3)	0.9174(3)	0.91643(5)	0.91648(5)	0.91657(5)
y(Ge5/Ge5′)	0.08460(5)	0.08461(6)	0.0860(2)	0.0873(3)	0.0873(3)	0.0873(3)	0.0871(3)	0.08461(6)	0.08460(6)	0.08460(6)
z(Ge5/Ge5′)	0.85276(5)	0.85287(5)	0.8530(2)	0.8544(3)	0.8542(3)	0.8542(3)	0.8541(3)	0.85282(5)	0.85278(5)	0.85277(5)
U_{eq}(Ge5) or U_{iso}(Ge5′)	0.0139(1)	0.0126(1)	0.0118(3)	0.0145(4)	0.0119(4)	0.0137(4)	0.0148(4)	0.0129(1)	0.0138(1)	0.0152(1)
Occ(Ge5″)	—	—	0.123	0.28	0.29	0.29	0.260	—	—	—
x(Ge5″)	—	—	0.911(1)	0.9086(7)	0.9078(7)	0.9082(7)	0.9086(7)	—	—	—
y(Ge5″)	—	—	0.075(1)	0.0779(7)	0.0782(7)	0.0781(7)	0.0777(8)	—	—	—
z(Ge5″)	—	—	0.853(1)	0.8532(8)	0.8537(7)	0.8536(8)	0.8535(8)	—	—	—
U_{iso}(Ge5″)	—	—	0.0118	0.0145	0.0119	0.0137	0.0148	—	—	—
x(Ge6)	0.18502(5)	0.18506(6)	0.18542(8)	0.1859(1)	0.1859(1)	0.1859(1)	0.1859(1)	0.18510(6)	0.18504(6)	0.18508(6)
y(Ge6)	0.98972(5)	0.98980(5)	0.99009(7)	0.9909(1)	0.9910(1)	0.9909(1)	0.9908(1)	0.98975(5)	0.98972(5)	0.98965(5)
z(Ge6)	0.87617(5)	0.87613(5)	0.87668(7)	0.8773(1)	0.8773(1)	0.8772(1)	0.8772(1)	0.87616(5)	0.87616(5)	0.87626(5)
U_{eq}(Ge6)	0.0129(1)	0.0110(1)	0.0106(2)	0.0137(3)	0.0111(3)	0.0130(3)	0.0139(3)	0.0115(1)	0.0122(1)	0.0137(1)

[a]Atom positions: Ba1 8*c* *x,x,x*; Ba1′ 24*e* *x,y,z*; Ba2′ 12*d* 1/8,*y*,*y* + 1/4; Ba2″ 24*e* *x,y,z*; Ba2‴ 24*e* *x,y,z*; Ba3′ 8*c* *x,x,x*; Ge1 24*e* *x,y,z*; Ge2 8*c* *x,x,x*; Ge3 8*c* *x,x,x*; Ge4 12*d* 1/8,*y*,*y* + 1/4; Ge4′ 12*d* 1/8,*y*,*y* + 1/4; Ge4″ 24*e* *x,y,z*; Ge5 24*e* *x,y,z*; Ge5′ 24*e* *x,y,z*; Ge5″ 24*e* *x,y,z*; Ge6 24*e* *x,y,z*. Occupancies for the split positions Ba1′ and Ba3′: Occ(Ba1′) = 1/3; Occ(Ba3′) = 1/2. The restrain Occ(Ba2′) + 2Occ(Ba2″) = 1 or Occ(Ba2′) + 2Occ(Ba2″) + 2Occ(Ba2‴) = 1 and the constrain U_{iso}(Ba2′) = U_{iso}(Ba2″) or U_{iso}(Ba2′) = U_{iso}(Ba2″) = U_{iso}(Ba2‴) were used for the components of Ba2. Also, the restrain Occ(Ge4′) = 1–2 Occ(Ge4″) = Occ(Ge5′) = 1–Occ(Ge5″) and the constrain U_{iso}(Ge5′) = U_{iso}(5″) were applied when necessary.

weak disordering of this atom positions which can be modelled using split sites. Upon cooling to temperatures below 225 K, the structural transformation involves further disorder of Ba2 and Ba3, combined with a gradual disordering of three other atomic positions (Ba1, Ge4 and Ge5). In the room temperature structure, Ba2 and Ba3 can be modelled rather accurately with anisotropic displacement parameters ($R_{gt}(F) = 0.037$), but in order to obtain comparable results for all temperatures, split positions were used to model Ba2 and Ba3 in the entire temperature range. The disordering of Ba1 is noticeable below 225 K, that of Ge4 below 250 K and that of Ge5 below 200 K (more details on these features are given below). A split model for each of these atoms was used in the respective refinement. The label of a disordered site is formed by adding to the name of the ideal position (Ba1, Ba2, Ba3, Ge4 and Ge5) the symbols ′ (prime), ″ (double prime) or ‴ (triple prime). Thus, the split site of the Ba1 atom (at 8*c* site) is called Ba1′ (24*e*), Ba2 (12*d*) is described by a central site Ba2′ (12*d*) and the satellites Ba2″ (24*e*) and Ba2‴ (24*e*), while the split position of Ba3 (4*a*) is named Ba3′ (8*c*) (see Figs. 5, 13, 14). The major and minor sites of Ge4 are called Ge4′ (12*d*) and Ge4″ (24*e*), respectively (see Fig. 7). Similarly, majority and minority components of Ge5 are labelled Ge5′ (24*e*) and Ge5″ (24*e*), respectively. In most cases, split positions were very close to each other, therefore equal isotropic displacement parameters were used for neighboring split sites to avoid strong correlations during refinement. The major component of Ge4 (Ge4′), which was well separated from the minor component, could be refined with anisotropic displacement parameters. In those cases where the occupancy became very small, the U_{iso} parameter was fixed at a suitable value. In all cases, the sum of the occupancies around each independent site was constrained to unity. As the disordering of Ge4 and Ge5 is correlated, the restrain $\mathrm{Occ(Ge4')} = 1–2\,\mathrm{Occ(Ge4'')} = \mathrm{Occ(Ge5')} = 1–\mathrm{Occ(Ge5'')}$ was used and the constrain $U_{iso}(\mathrm{Ge5'}) = U_{iso}(\mathrm{Ge5''})$ was added. Furthermore, the three components of Ba2 were restrained using SUMP in SHELXL-97. For data sets obtained at certain temperatures ($205\,\mathrm{K} < T < 250\,\mathrm{K}$), it was not possible to refine the split model for Ge5. In these cases only the averaged position of Ge5 was refined.

Crystallographic data and atomic coordinates of Ba_6Ge_{25} for some selected temperatures in the range 95–295 K (cool-down and heat-up sweeps) are presented in Table 1.[1] Difference electron densities in the vicinity of the crucial atom positions are shown in Figs. 5 and 7, the variation of their occupancies as a function of temperature is illustrated in Fig. 6. Distances between an atom position and two symmetry-related positions are differentiated by using labels *d*1 and *d*2 (see Figs. 8 and 9). However, in certain cases a more detailed labelling scheme had to be used (see Figs. 10, 12, 15 and 16).

According to our single-crystal diffraction experiments the structure around the Ba positions remains practically unchanged on cooling until about 225 K (Fig. 5). For temperatures below 225 K, a gradual deformation in the difference electron density around Ba1, Ba2 and Ba3 positions is observed as a function of temperature. Depending on the temperature range, one initial site, one split site or even an additional split site are required to properly model the electron density around those atoms. One of the most interesting features observed below 225 K is the appearance of the second split site Ba2‴ in the vicinity of Ba2 (described by Ba2′ and Ba2″ sites at $T > 225$ K). This effect coincides with step *S1* of the phase transformation. Electron density around Ba3 again stays almost unchanged until $T = 225$ K, before it starts to deform, and finally at $T = 175$ K the deformation increases rapidly. This feature defines step *S2* of the transformation.

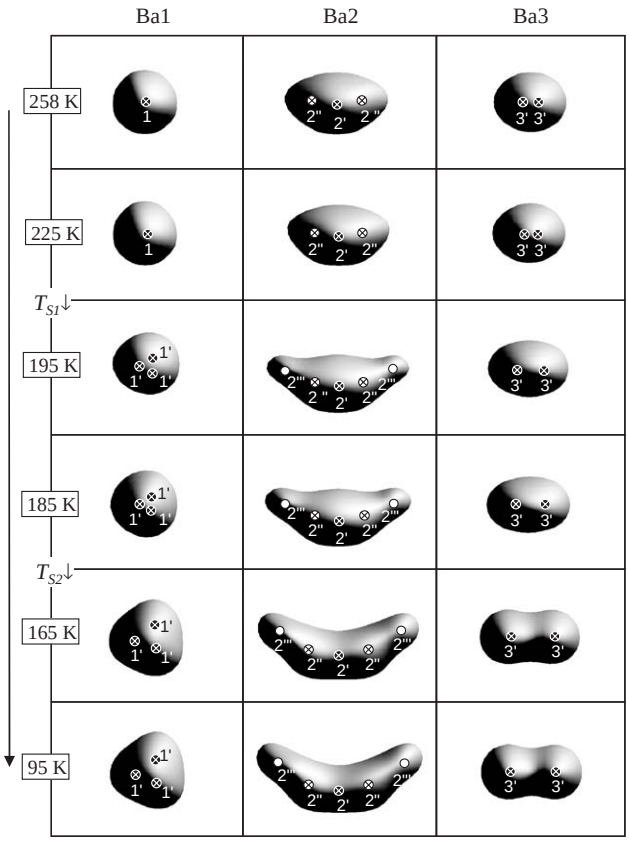

Fig. 5. Difference electron density (isosurface at 11e/Å^3) around Ba1 (left), Ba2 (middle) and Ba3 (right) sites in Ba_6Ge_{25} as a function of temperature (cooling sweep). For an appropriate description of the electron density, split barium sites (marked in the figure) are required.

[1]The atomic coordinates for all temperatures and other details were deposited at the Fachinformationszentrum Karlsruhe (D-76344, Eggenstein-Leopoldshafen, Germany; crysdata@fiz-karlsruhe.de) and are available quoting the names of the authors, citation paper, the measurement temperature and the depository numbers CSD-414371 to 414396.

Similar changes are observed on the electron density around Ba1, which splits first into three symmetry-related Ba1′ sites at T_{S1}(down) before it strongly expands at T_{S2}(down). Below T_{S2}(down) changes in the electron density for all Ba sites are relatively small.

On cooling, the occupancy of Ge4′ (12*d*) site is reduced starting at 250 K (Fig. 6a; the occupancies of Ge4 and Ge4′ are plotted together). Parallel to this reduction the new split site Ge4″ (24*e*) appears near the main Ge4′ site (Fig. 7). Because the distances *d*(Ge4′–Ge4″) and *d*(Ge4″–Ge4″) between neighboring Ge4′ and Ge4″ sites are quite short at 1.19(9) Å–1.39(1) Å and 1.8(2)–2.14(3) Å, respectively, they cannot be occupied at the same time. The occupation of Ge4″ sites starts at 250 K defining the step S_0 of the transformation. At 225 K a clear change in the gradient of the curve $Occ_{Ge4/Ge4'}(T)$ is observed. Below 180 K ($\approx T_{S2}$(down)) the Ge4′ occupancy is severely reduced to about 72(1) % at 175 K, but remains almost unchanged by cooling further to 95 K. The occupancy of Ge4″ site increases complementary from 0% at 250 K to 14.6% at 95 K. These effects are reversible with hysteresis.

Between T_{S1} and T_{S2} the electron density at the central region around Ba2 (Ba2′ site) decreases with

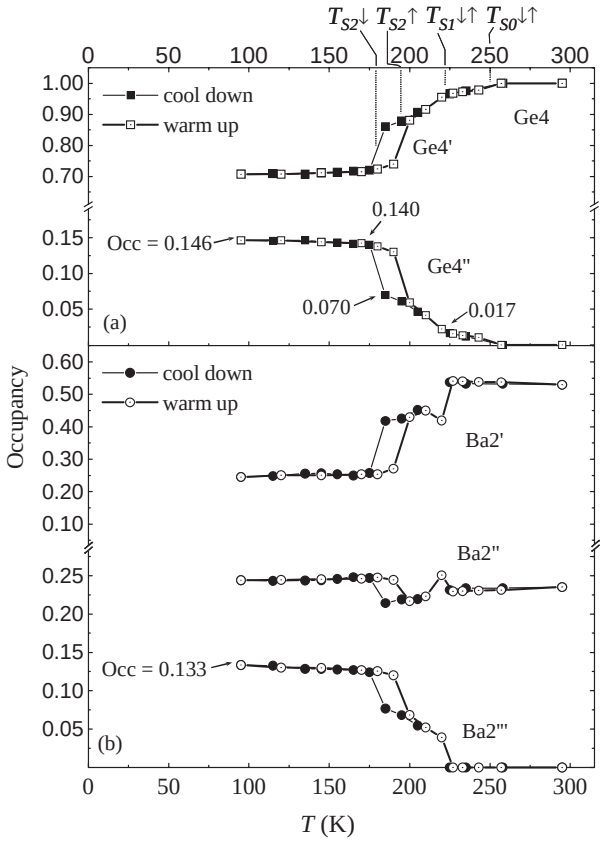

Fig. 6. Site occupancies as a function of temperature (cooling and warming sweeps) for the sites Ge4/Ge4′ and Ge4″ (a), and Ba2′, Ba2″ and Ba2‴ (b). The values for Ge4 and Ge4′ are plotted together.

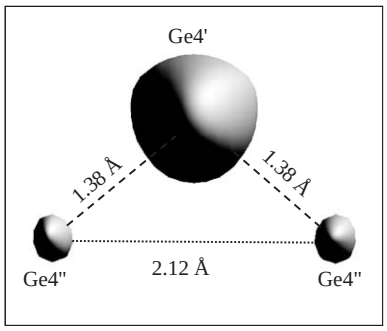

Fig. 7. Difference electron density (isosurface at 7e/Å^3) around the Ge4 site in Ba_6Ge_{25} at 165 K.

lowered temperature. At the same time, electron density at the outer region (Ba2‴) increases with decreasing temperature (Fig. 5). This behavior is well reflected by the corresponding site occupancies (Fig. 6b). Occupancies of Ba2′ and Ba2″ are practically constant until about 225 K, change stepwise at 205 and 175 K, before they again remain unchanged by further cooling to 95 K. The outer component Ba2‴ first appears at 225 K. Its occupancy increases stepwise but complementary to Ba2′ and Ba2″. In the warm-up cycle the reverse effect with thermal hysteresis at about 185 K is observed.

In a preliminary refinement stage (using the average Ge5 position) examination of the Ge–Ge bond lengths for the split Ge4″ site indicated unusually short distances (2.30–2.33 Å) for one out of two Ge4″–Ge5 bonds. Inspection of the anisotropic displacement parameters of neighboring Ge5 atoms indicated possible splitting (U_{11} component became larger with decreasing temperature). As mentioned above, a splitting model for Ge5 (Ge5 → Ge5′ + Ge5″) was introduced in the refinements for $T \leqslant 200$ K (in the range 205–250 K the splitting of Ge5 is too small to be resolved). In this way, more acceptable lengths for both bonds (*d*1(Ge4″–Ge5″) and *d*2(Ge4″–Ge5″)) were obtained. Notice, in a local range model the major component Ge5′ is associated with neighboring Ge4′ sites and the minor component Ge5″ is associated with neighboring Ge4″ sites (see ordered model in Fig. 11).

Selected Ge–Ge bond lengths as a function of temperature are presented in Fig. 8. They are affected in different ways by the transformation. While some distances, e.g. *d*1(Ge1–Ge6), *d*2(Ge1–Ge6) and *d*(Ge4′–Ge5′)/*d*(Ge4–Ge5) show only slight changes with temperature, other distances show stronger temperature dependence with thermal hysteresis at about 185 K. Most interesting are those distances which increase with decreasing temperature and appear to be related to the anomalous behavior of the lattice parameter, e.g. *d*(Ge2–Ge2) increases in two steps. The latter first decreases to 2.497(2) Å at 225 K, increases slowly to 2.508(4) Å at 185 K, further increases abruptly below 180 K (2.522(5) Å at 175 K), but remains almost

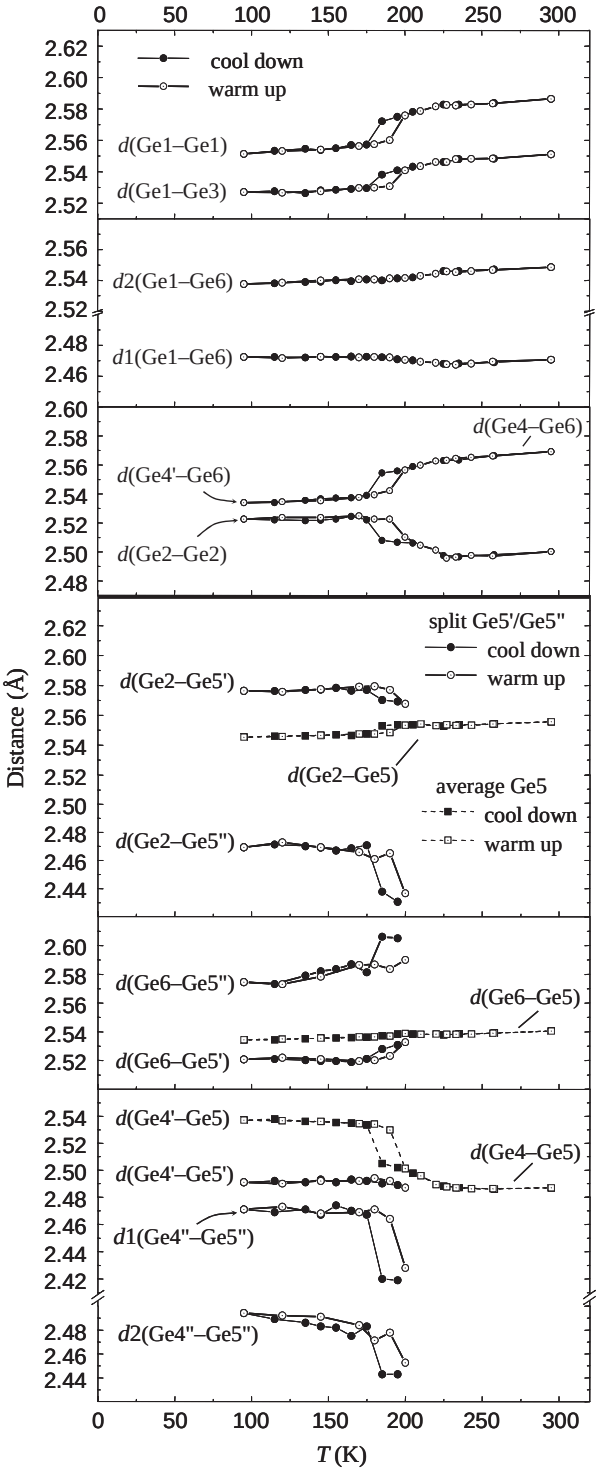

Fig. 8. Selected d(Ge–Ge) bond distances in Ba_6Ge_{25} as a function of temperature. Ge4 → Ge4′ + Ge4″ ($T < 245$ K). Ge5 → Ge5′ + Ge5″ ($T \leqslant 200$ K). Distances related to Ge4 and Ge4′ are plotted together.

constant below 170 K. During warm up the reverse effect with hysteresis is observed.

To simplify the description of the phase transformation in this relatively large crystal structure, the analysis of d(Ba–Ge) and d(Ba–Ba) distances is mostly limited to the *average* positions Ba1, Ba3 and Ge5, and the Ba2′ position (Fig. 9). In order to describe the main temperature variations in the germanium environment around the Ba positions, key germanium atoms were chosen. The pentagonal dodecahedron around Ba1 decreases in size by cooling down, the average distances from Ba1 to Ge1, Ge4′ and Ge5 also decrease in different degrees on cooling (not shown in Fig. 9). The strongest decrease is observed for the d(Ba1–Ge3) distance. The Ba3 coordination *cube* (Fig. 9, bottom) increases in size with decreasing temperature and the change of d(Ba3–Ge3) is the most dramatic. The behavior of the Ba2 environment is more complex (Fig. 9, middle). On cooling, it elongates along the direction of the Ba2 shifting (see d(Ba2′–Ge4/4′), $d2$(Ba2′–Ge5) and d(Ba2′–Ge6)), but shrinks along other directions (e.g. d(Ba2′–Ge1), d(Ba2′–Ge3)). As the

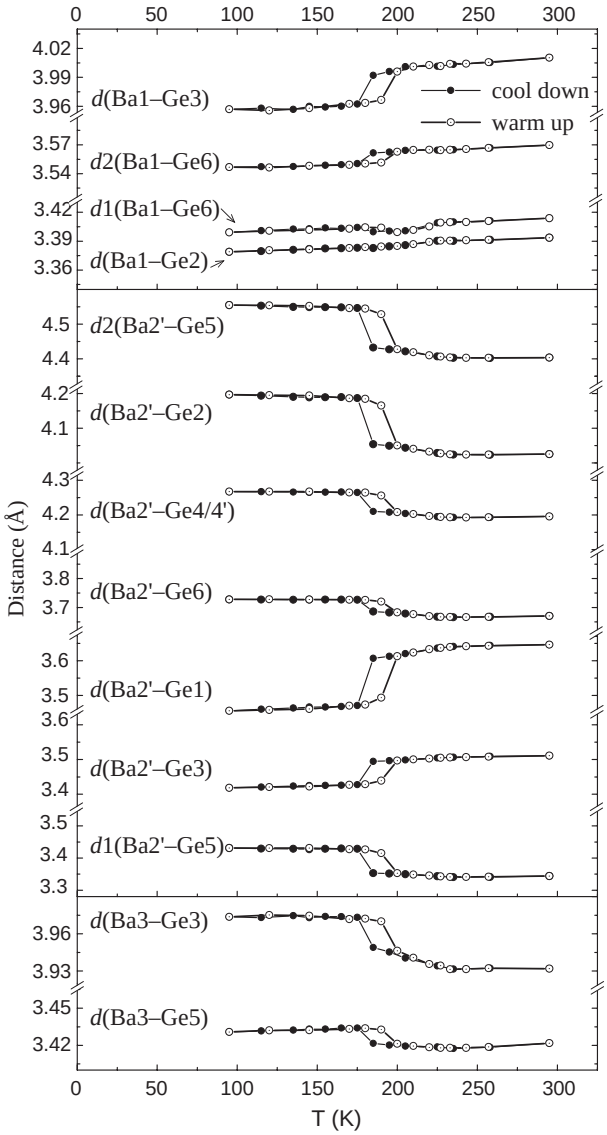

Fig. 9. Relevant d(Ba–Ge) distances for the average positions Ba1 (top), Ba2′ (middle) and Ba3 (bottom) as a function of temperature.

central Ba2′ moves away from Ge2 towards Ge1, the relative changes on d(Ba2′–Ge2) and d(Ba2′–Ge1) are opposite and large. The effective change of the Ba2 polyhedron along the Ge1···Ge2 direction is a contraction (d(Ge1···Ge2) varies from 7.405(1) Å at 295 K to 7.383(2) Å at 95 K).

Selected average d(Ba–Ba) distances are shown as function of temperature in Fig. 10. These distances were chosen to follow the main variations of the barium environment around the Ge4″ site. The strongest temperature effect is observed for the d_A(Ba1–Ba2′) distance, increasing rapidly on cooling. It is interesting that the shortest average distance d(Ba2′–Ba3) (4.626(1)–4.676(3) Å) increases on cooling, as it is correlated to the enlargement of the Ba3 *cube*. On the contrary, the d(Ba1–Ba1) distance is remarkably insensitive to the phase transformation.

3.3. Mechanism of the structure transformation

As was shown by the analysis of site occupancies and interatomic distances, the transformation comprises disorder at some sites of the germanium framework combined with disordering in the barium substructure. In order to discuss and understand the reconstruction of the structure we introduce local order models for the relevant fragments of the structure.

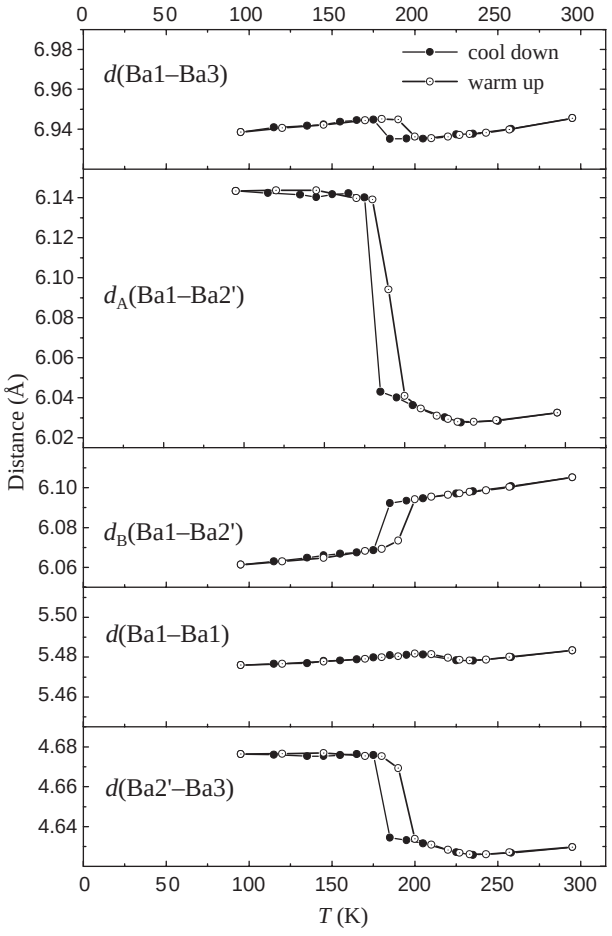

Fig. 10. Selected d(Ba—Ba) distances between the average positions Ba1, Ba3, and the central Ba2′ site as a function of temperature (d_A and d_B are defined in Fig. 12).

The shifting of about 25% of the Ge4 atoms towards the Ge4″ position at $T<250$ K is very pronounced (1.19(9)–1.39(1) Å, depending on temperature; Fig. 7). This feature is the most important finding in the present study and it means that *one* out of four Ge4 atoms is displaced in course of the transition, causing *one* of four Ge6–Ge4 bonds to break (Fig. 11). A second set of Ge6–Ge4 bonds remains unchanged. This demands a local symmetry breaking (the two-fold axis passing through Ge4 (12*d*) site is removed). Consequently, *one new* three-bonded (3b)Ge^- at Ge4″ and *one new* three-bonded (3b)Ge^- at Ge6 sites are formed, associated with the formation of eight-membered rings in the germanium framework (Fig. 11b, bottom).

The bond-breaking mechanism described above could in principle involve all four-bonded Ge positions (Ge1, Ge2, Ge4 and Ge6). However, analysis of the room temperature structure of Ba_6Ge_{25} reveals that only Ge4 has the appropriate environment for bond breaking. In contrast to Ge1, Ge2 and Ge6 (all at centres of Ba_4 tetrahedra), Ge4 is located at the centre of a Ba_5 triangular bipyramid (Fig. 12), disclosing relatively large distances of 4.190(1) and 4.244(1) Å to Ba2 and Ba3 sites, respectively ($T=295$ K). Moving to the neighboring tetrahedral site (Ge4″), Ge4 pushes its Ba2 neighbor to the Ba2‴ position (with d(Ge4″–Ba2‴) = 3.774(2) Å and d(Ge4″–Ba3′) = 3.50(2) or 3.66(2) Å, at 165 K). This interpretation is supported by the correlation of the occupancies of Ge4″ and Ba2‴ positions in the temperature range 95–222 K: the shift Ge4 → Ge4″ occurs simultaneously with the displacement Ba2′ → Ba2‴. A local order model for this process is depicted in Fig. 13. However, a shift Ba2′ → Ba2″ combined with a second shift Ba2″ → Ba2‴ (leaving the relative occupancy of Ba2″ constant) is also possible. Local changes in the environment of Ba1 and Ba3 sites, as a consequence of the Ge4 → Ge4″ shifting, are presented in Fig. 14.

We believe that the 'driving force' for this transformation is the relatively high excess charge in Ba_6Ge_{25} (4e^- per formula unit; cf. Introduction). This situation becomes unstable at temperatures below 250 K, giving rise to a reduction of excess charge down to about 2.2 e^-. Considering the *new*ly created (3b)Ge^- species (due to the Ge4 shifting) in the Zintl-Klemm electron count, the charge balance for Ba_6Ge_{25} at $T<250$ K can be formulated as $[Ba^{2+}]_6[(3b)Ge^-_{old}]_8[(3b)Ge^-_{new}]_{(4-n)}[(4b)Ge^0]_{17-(4-n)}[ne^-]$ ($n\approx 2.2$ at 95 K).

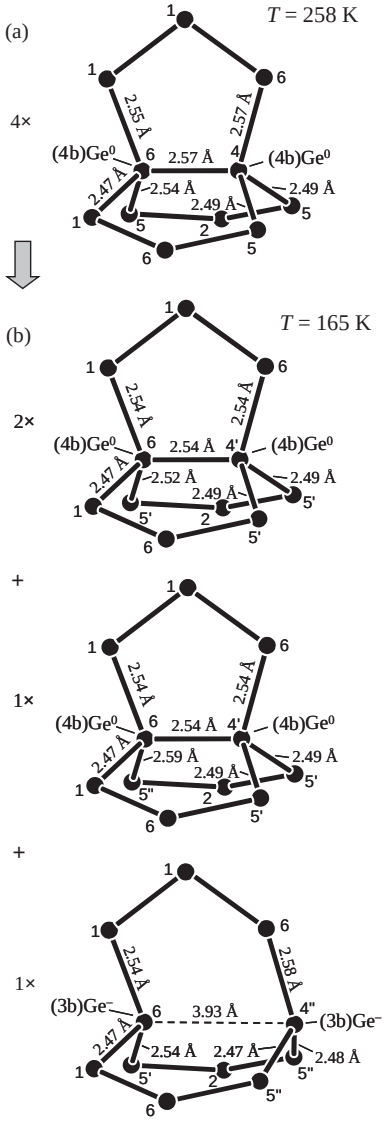

Fig. 11. Temperature induced structural changes in the Ge network of Ba_6Ge_{25}. (a) Selected fragment consisting of three condensed five-membered Ge-rings above the transition ($T = 258$ K). (b) Models of basically unchanged ($3\times$) and rearranged ($1\times$) fragments after the transition (at 165 K) representing a breaking of one Ge6–Ge4 bond. Creation of two *new* three-bonded (3b)Ge^- species: one at Ge6 and one at Ge4″ (bottom).

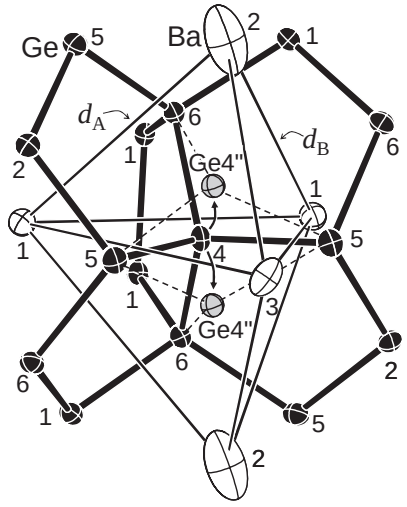

Fig. 12. Barium (white ellipsoids) and germanium (black) environments around the four-bonded (4b) Ge4 atom at $T = 295$ K. A Ba_5 triangular bypyramid is centred by Ge4. The split positions Ge4″ (gray) appear below 250 K. Ge4 → Ge4″ shifts are indicated.

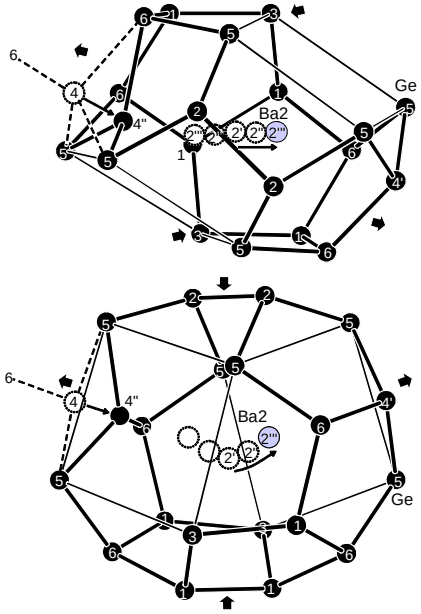

Fig. 13. Two views of the germanium environment around Ba2 position showing a local ordering model for Ge4″ and Ba2‴ positions at temperatures below 220 K (average Ge5 position was used for the drawing). Thin arrows indicate the main atomic shifts, and the thick arrows denote the main expansion or compression by cooling.

3.4. Lattice parameter anomalies

The bond-breaking/(3b)Ge^--creation mechanism is the main reason for the increase of the lattice parameter $a(T)$ observed in the range 240–180 K (Fig. 5a). An increase of the unit cell volume is necessary to accommodate the three-bonded (3b)Ge^- species, which are demanding space for their active lone-pairs ('dangling bonds').

The collective effect of the structural changes caused by the Ge-bond-breaking/Ba-shifting on the lattice parameter $a(T)$ can be analyzed with the help of a structural fragment aligned along the [111] direction, containing two Ba1 at Ge_{20} pentagonal dodecahedra (Ba1-*pdos*) connected by a Ge2–Ge2 bridge and one Ba3 at Ge_8 polyhedron with six additional neighboring Ba2 atoms (Fig. 15). The Ge2–Ge2 bridge (with $d_{22} = d$(Ge2–Ge2)), the Ge2–Ba1–Ge3 segment (with $L_{23} = d$(Ge2···Ge3)) and the Ge3–Ba3–Ge3 diagonal

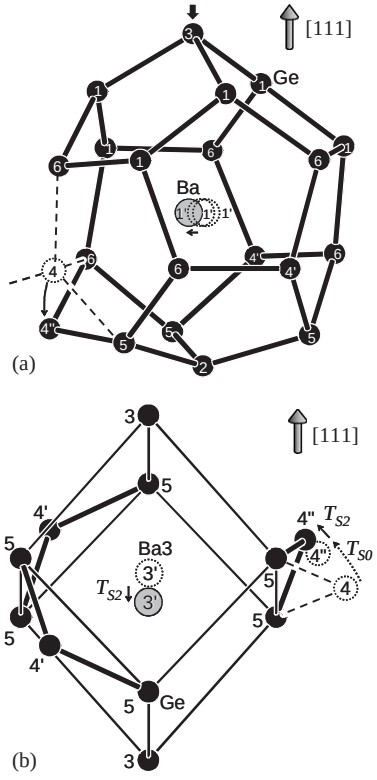

Fig. 14. Germanium environment of Ba1 (a) and Ba3 (b), illustrating a local ordering model concerning the influence of Ge4 shifts on the Ba1 and Ba3 environments at T below 220 K (average Ge5 position was used for the drawing). Main atomic shifts are indicated by thin arrows. In (b), the shift of Ge4 to Ge4″ at $T_{SO} \approx 250$ K, thin dashed arrow, and at T_{S2}, thin solid arrow, are emphasized (latter Ge4 shift is correlated with main shift of Ba3 to Ba3′). The thick black arrow in (a) indicates the main compression by the transition.

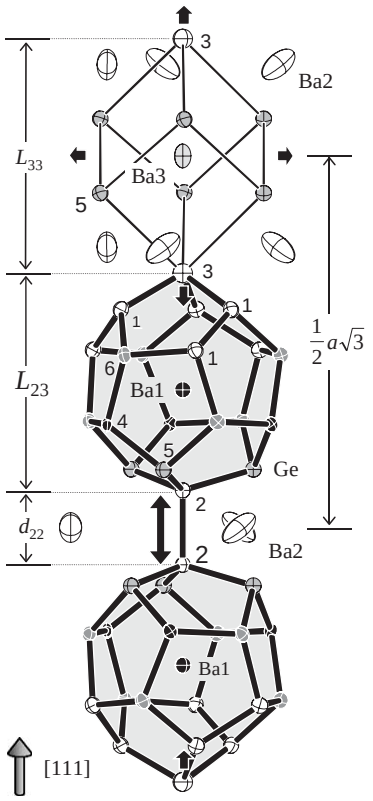

Fig. 15. Extended fragment of the Ba_6Ge_{25} structure oriented along [111] direction. The fragment consists of one Ba3-*cube* sharing a corner with a Ba1-*pdo* which is further connected to another Ba1-*pdo* by a Ge2–Ge2 bridge. The surrounding Ba2 atoms are also shown. The thick black arrows indicate main expansion directions induced by cooling down through the phase transition. Some distances are defined (L_{33}, L_{23}, d_{22}) or indicated ($1/2a\sqrt{3}$) in the figure.

(with $L_{33} = d(\mathrm{Ge3}\cdots\mathrm{Ge3})$) are subsequent segments in the chain aligned along [111] as depicted in Fig. 15. The sum $2L_{23} + L_{33} + d_{22}$ is equal to the length of the body diagonal of the cubic unit cell, and therefore $a = [2L_{23} + L_{33} + d_{22}]/\sqrt{3}$. In order to extract the contributions of these three components to the changes of the lattice parameter, the values of $2L_{23}/\sqrt{3}$, $L_{33}/\sqrt{3}$ and $d_{22}/\sqrt{3}$ are plotted as a function of temperature together with those of the weighted sum $[2L_{23} + L_{33} + d_{22}]/\sqrt{3}$ in Fig. 16. The temperature dependence of the partial sum $[2L_{23} + L_{33}]/\sqrt{3}$ $(= d(\mathrm{Ge2} - \mathrm{Ba1} - \mathrm{Ge3} - \mathrm{Ba3} - \mathrm{Ge3})/\sqrt{3})$ is also drawn, representing the net effect of the combined interactions among Ba1 (Ba3) and Ge2/Ge3 (Ge3). Every component contributes in different ways to the variations observed for the lattice parameter. In particular, $2L_{23}/\sqrt{3}$ and $L_{33}/\sqrt{3}$ show dramatic changes with temperature, but both changes almost cancel each other. The main anomalies on the lattice parameter at T_{S1} and T_{S2} are driven by the variation of d_{22} (related to the movements of Ba2) and to a smaller extend by those of $[2L_{23} + L_{33}]$ (representing Ba1/Ba3 ↔ Ge2/Ge3 interactions).

3.5. Relationship between structural transformation and peculiarities of the electrical resistivity and magnetic susceptibility

A main consequence of breaking the Ge4–Ge6 bonds is the creation of *electron acceptors* where excess electrons are used to form three bonded (3b)Ge^- species. For example, an occupancy factor of 0.72 for Ge4′ (12*d*) at 175 K means that 0.84 Ge4 atoms per formula unit are shifted to Ge4″ (24*e*) sites, while moving away from one Ge6 neighbor. This creates (per formula unit) 0.84 (3b)Ge^- at Ge4″ and 0.84 (3b)Ge^- at Ge6 sites. According to the Zintl-Klemm electron count and assuming normal single bonds, this model requires 1.68 electrons and implies the reduction of excess electrons per Ba_6Ge_{25} formula unit from 4 at room temperature to 2.32 at 175 K (cf. Section 3.3). Based on refined site occupancies, this model permits to calculate the number of excess electrons n per formula unit for the entire temperature range (Fig. 17).

The variation of $n(T)$ influences all physical properties. The lattice irregularities induced by the transformation increase the rate of electron scattering, but also

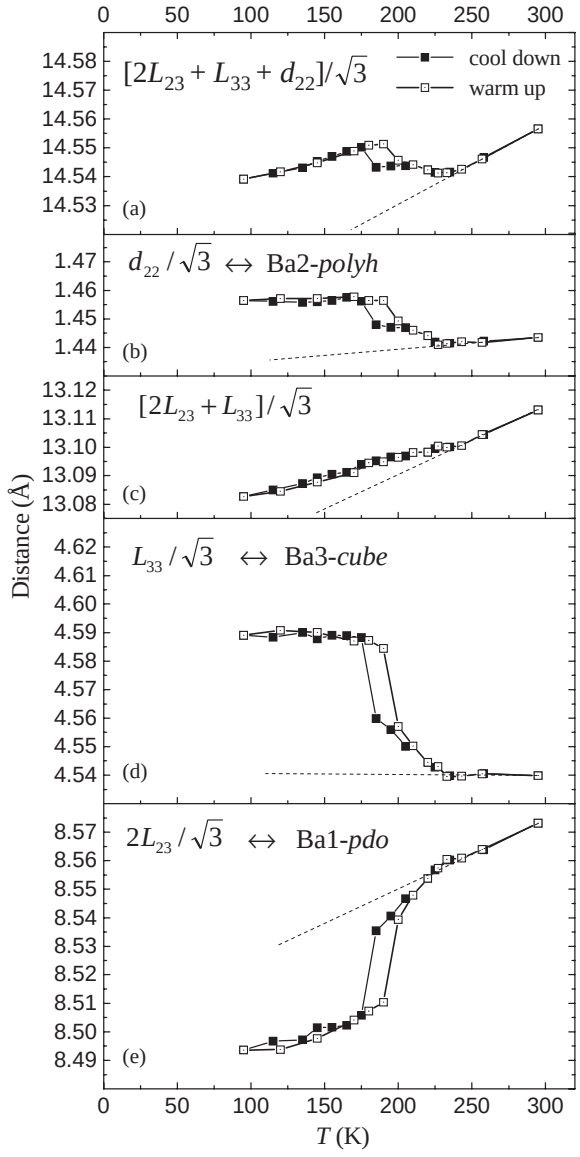

Fig. 16. Temperature dependence of (a) the weighted sum $[2L_{23}+L_{33}+d_{22}]/\sqrt{3}$, (b) $d_{22}/\sqrt{3}$, (c) the weighted sum $[2L_{23}+L_{33}]/\sqrt{3}$, (d) $L_{33}/\sqrt{3}$and (e) $2L_{23}/\sqrt{3}$ (cooling and warming-up sweeps). The distances d_{22}, L_{33}, and L_{23} are defined in Fig. 15. The dashed lines are drawn to emphasize the relative changes at $T<250$ K (cf. Fig. 4).

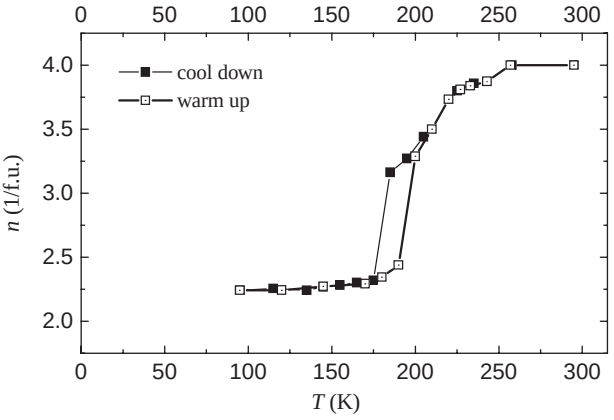

Fig. 17. Temperature dependence of the number of excess electrons n per formula unit calculated according to the Zintl-Klemm concept.

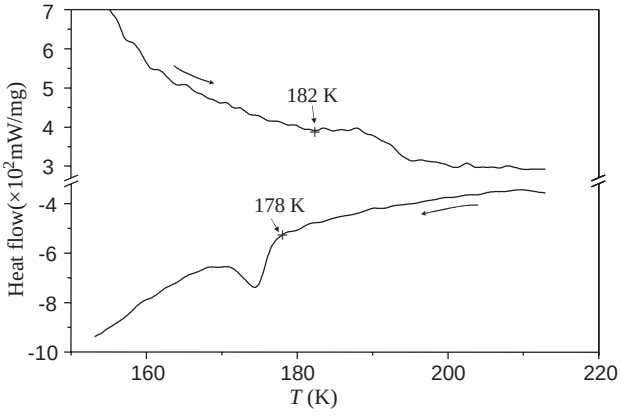

Fig. 18. Temperature dependence of the DSC signal (5 K/min) for Ba_6Ge_{25}.

reduce electron mobility. Reduction of both concentration and mobility of charge carriers reduces the electrical conductivity in two steps at T_{S1} and T_{S2} [8]. Nevertheless, even below T_{S2} the resistivity should remain metal-like, however, a semiconductor-like behavior is observed. This may be explained by directional interaction between Ba atoms and neighboring (4b)Ge atoms. The very same arguments hold also for the two-step reduction of the magnetic susceptibility.

The complex structural changes spread over a broad temperature range allow to understand the unusually wide form of the anomaly peak in specific heat $c_p(T)$ measurements. The disorder model at lower temperatures is well in accordance with the relatively large entropy change associated with this phase transformation [8]. The phase transition was further checked by DSC measurement (Fig. 18). On heating, a broad endothermic peak with onset at about 182 K is observed, while on cooling the respective exothermic peak (~1.8 kJ/mol) shows an onset at about 178 K.

The symmetrical anomaly in the specific heat measurement and the observed thermal hysteresis effects are indicative of a first-order phase transition [8]. However, the structural changes observed in this transformation at atomic level, such as Ge–Ge bond breaking combined with excess-charge reduction, are characteristic features of a solid-state chemical reaction in which internal redox processes or redistribution of charges are involved.

4. Conclusions

In the temperature range 10–295 K Ba_6Ge_{25} retains cubic translation symmetry and space group $P4_132$ is

used to describe the crystal structure throughout. The low-temperature structure transformation is of reconstructive nature. The germanium host framework as well as barium guest atoms are involved in this process. The "driving force" seems to be the relatively high excess of charge carriers in the structure at room temperature, i.e. $4\,e^-$ per formula unit as deduced from the Zintl-Klemm electron count. At temperatures above 225 K the Ge framework contains 17 four-bonded (4b) and eight three-bonded (3b) Ge atoms per formula unit. Cooling causes breaking of one of the two Ge4–Ge6 bonds per Ge4 atom and leaves the associated germanium atoms only three-bonded. This formation of (3d)Ge^- species leads to the reduction of excess charges from 4 e^- per formula unit to about 2.24 e^- at 95 K. As a consequence of the Ge4 displacement the Ba atoms are also shifted inside the cages of the Ge framework.

The bond breaking with the formation of dangling bonds and the respective displacement of Ba atoms helps to explain the two-step expansion of the unit cell upon cooling. During warm-up, all related phenomena are reversed with hysteresis.

Formation of dangling bonds and accompanying shifts of the barium atoms explain the main variations of electrical resistivity and magnetic susceptibility during and after the phase transformation in Ba_6Ge_{25}.

Finally, the Ge–Ge bond breaking combined with the reduction of excess-charges represents a solid-state chemical reaction. To our knowledge, this is the first observation where covalent Ge–Ge bonds are broken at low temperatures in a solid-state reaction.

Acknowledgments

The authors thank Dr. G. Auffermann, Mr. O. Prim and Mrs. U. Schmidt for the chemical analyses, Dr. R. Ramlau and Mrs. P. Scheppan for the SEM/EDX investigations and Dr. R. Niewa and Mrs. S. Müller for the DTA/DSC measurements.

References

[1] W. Carrillo-Cabrera, J. Curda, H.G. von Schnering, S. Paschen, Yu. Grin. Z. Kristallogr. NCS 215 (2000) 207.
[2] H. Fukuoka, K. Iwai, S. Yamanaka, H. Abe, K. Yoza, L. Häming. J. Solid State Chem. 151 (2000) 117.
[3] S.J. Kim, S. Hu, C. Uher, T. Hogan, B. Huang, J.D. Corbett, M.G. Kanatzidis, J. Solid State Chem. 153 (2000) 321.
[4] R. Kröner, R. Nesper, H.G. von Schnering, Z. Kristallogr. NCS 182 (1988) 164.
[5] H.G. von Schnering, R. Kröner, W. Carrillo-Cabrera, K. Peters, R. Nesper, Z. Kristallogr. NCS 213 (1998) 665.
[6] W. Klemm, Proc. Chem. Soc. London (1958) 329.
[7] H. Schäfer, Ann. Rev. Mater. Sci. 15 (1985) 1.
[8] S. Paschen, V.H. Tran, M. Baenitz, W. Carrillo-Cabrera, Yu. Grin, F. Steglich, Phys. Rev. B 65 (2002) 134–435.
[9] S. Paschen, W. Carrillo-Cabrera, M. Baenitz, V.H. Tran, A. Bentien, H. Borrmann, R. Cardoso Gil, R. Michalak, Yu. Grin, F. Steglich, Development of the Institute and Scientific Report, Max-Planck-Institut für Chemische Physik fester Stoffe, November 2000, p. 71.
[10] F.M. Grosche, H.Q. Yuan, W. Carrillo-Cabrera, S. Paschen, C. Langhammer, F. Kromer, G. Sparn, M. Baenitz, Yu. Grin, F. Steglich, Phys. Rev. Lett. 87 (2001) 247003.
[11] H.Q. Yuan, F.M. Grosche, W. Carrillo-Cabrera, S. Paschen, C. Langhammer, G. Sparn, M. Baenitz, Yu. Grin, F. Steglich, High Pressure Res. 22 (2002) 147.
[12] H.Q. Yuan, F.M. Grosche, W. Carrillo-Cabrera, S. Paschen, C. Langhammer, G. Sparn, M. Baenitz, Yu. Grin, F. Steglich, J. Phys.: Cond. Matter 14 (2002) 11249.
[13] (a) V. Petkov, T. Vogt, Solid State Commun. 127 (2003) 43;
(b) M. Schmidt, P.G. Radaelli, M.J. Gutmann, S.J.L. Billinger, N. Hur, S.W. Cheong, J. Phys.: Cond. Matt. 16 (2004) 7287.
[14] W. Carrillo-Cabrera, J. Curda, K. Peters, S. Paschen, Yu. Grin, H.G. von Schnering, Z. Kristallogr. NCS 215 (2000) 321.
[15] R.F.W. Herrmann, K. Tanigaki, T. Kawaguchi, S. Kuroshima, O. Zhou, Phys. Rev. B 60 (1999) 13245.
[16] L.G. Akselrud, P.Y. Zavalii, Yu.N. Grin, V.K. Pecharskii, B. Baumgartner, E. Wölfel, CSD, an universal program package for single crystal and/or powder structure data treatment, Mater. Sci. Forum 133–139 (1993) 335.
[17] X-RED 1.10, STOE Data Reduction Program, STOE & Cie GmbH, Darmstadt, 1998.
[18] G.M. Sheldrick, SHELXL-97. Program for refining of crystal structures, University of Göttingen, Germany, 1997.
[19] (a) L.J. Farrugia, J. Appl. Crystallogr. 32 (1999) 837
(b) L.J. Farrugia, WinGX—Version 1.64.05, An Integrated System of Windows Programs for the Solution, Refinement and Analysis of Single Crystal X-ray Diffraction Data. Department of Chemistry, University of Glasgow, 1997–2003.
[20] E.B. Sokolov, V.M. Glazov, V.K. Prokof'eva, Izv. Akad. Nauk. SSSR, Neorg. Mater. 6 (1970) 580.
[21] G. Petzow, G. Effenberg, Ternary Alloys, Vol. 3, VCH Verlagsgessellschaft, Weinheim, Germany, 1990, pp. 266–268.
[22] W. Carrillo-Cabrera, S. Budnyk, Yu. Prots, Yu. Grin, Z. Anorg. Allg. Chem. (2004) 2267.
[23] Y. Murakani, H. Shibuya, D. Shindo, J. Microscopy 203 (2001) 22.